Polymer electrolyte fuel cell modeling - A comparison of two models with different levels of complexity

S. Zhang^a, S. B. Beale^{a,b,*}, U. Reimer^a, M. Andersson^d, W. Lehnert^{a,c,e}

Abstract

performance calculations for high-temperature fuel cells, have typically been obtained by two distinct computational methods; either by applying a simple kirchhoff-ohm relationship in two-dimensions, or by solving detailed threedimensional poisson equations. the motivation for this study was to compare quantitively the results of the two models, not only by comparison with each other, but also with detailed experimental data. the novelty is that this is the first such comparison to be undertaken. key results include the observation that both models can predict overall performance and current density distributions, with good agreement. when local current densities are compared, slight differences in extrema are observed, however by-and-large, the results are mutually consistent. the simpler method cannot capture the three-dimensional nature of the current density distribution throughout the interior of the fuel cell. therefore, if the required additional computational power is available, a more comprehensive picture can be obtained from the detailed model. however, the simpler model may also be used as a predictive tool. the present contribution to the literature was obtained for a polymer electrolyte fuel cell, however

^a Forschungszentrum Jülich GmbH, IEK-3: Electrochemical Process Engineering, 52425 Jülich, Germany

^b Mechanical and Materials Engineering, Queen's University, Kingston ON K7L 3N6, Canada

^cRWTH Aachen University, Faculty of Mechanical Engineering, 52062 Aachen, Germany ^dDepartment of Energy Sciences, Lund University, P.O. Box 118, SE-221 00, Lund, Sweden ^eJARA-HPC, 52425 Jülich, Germany

^{*}Corresponding author, Tel: +49 2461 61-8856.

Email addresses: s.zhang@fz-juelich.de (S. Zhang), s.beale@fz-juelich.de (S. B. Beale), u.reimer@fz-juelich.de (U. Reimer), martin.andersson@energy.lth.se (M. Andersson), w.lehnert@fz-juelich.de (W. Lehnert)

the conclusions may readily be applied to other high temperature fuel cells.

 $\it Keywords\colon$ fuel cell, mathematical modeling, computational fluid dynamics, current density

${\bf Nomenclature}$

English

- C Molar concentration, mol m⁻³
- C_p Specific heat, $J kg^{-1} K^{-1}$
- $D_{\rm i}^{\rm eff}$ Effective diffusion coefficient, m² s⁻¹
- $E_{\rm n}$ Nernst potential, V
- F Faraday's constant, $C \operatorname{mol}^{-1}$
- H Enthalpy, $J \text{ mol}^{-1}$
- h Thickness, m
- i Current density, A cm⁻²
- i_0 Exchange current density, A m⁻³ or A cm⁻²
- J_{φ} Electronic/protonic source term, A m⁻³
- K Permeability, m⁻²
- $k^{\rm eff}$ Effective thermal conductivity, W m⁻¹ K⁻¹
- n Number of electron transfer
- p Pressure, Pa
- Q Heat source, W m⁻³
- R Ohmic resistance, Ω cm²; mass source/sink, kg m⁻³ s⁻¹
- R_g Universal gas constant, $J \text{ mol}^{-1} K^{-1}$

- $S \qquad \quad {\rm Entropy, \ J \, mol^{-1} \, K^{-1}}$
- T Temperature, K
- ${f U}$ Velocity, m s⁻¹
- V Voltage, V
- Y Mass fraction

Greek

- α Transfer coefficient
- η Activation overpotential, V
- γ Power exponent
- λ Stoichiometric factor
- μ Viscosity, kg m⁻¹ s⁻¹
- ω Relaxation factor, $\Omega \, \mathrm{cm}^2$
- ϕ Potential, V
- ρ Density, kg m⁻³
- σ Electrical conductivity, S m⁻¹

1. Introduction

The polymer electrolyte fuel cell (PEFC) is a promising energy conversion device that directly converts chemical energy into electricity with high efficiency and no polluting emissions. It has attracted much attention [1–6] in recent decades, and great technical advances have been achieved, such as catalyst loading being greatly reduced, power density increasing and new industrial applications being identified. However, the commercialization of PEFCs for mobile

and stationary applications is still limited by several technical issues, including water and thermal management, impurities of carbon monoxide, sluggish electrochemical cathode kinetics and the high-cost of components [5].

A phosphoric acid doped polybenzimidazole (PBI) membrane is employed in HT-PEFCs. In light of this, high-temperature PEFCs (HT-PEFCs), which operate at temperatures of 140 – 180 °C, provide an alternative way to solve the aforementioned issues. Due to their high operating temperatures, water only exists in the vapor phase, which means that the flooding problem in conventional PEFCs does not arise and water management is much easier by comparison to conventional PEFCs. Another consequence of the high operating temperature is the high carbon monoxide (CO) tolerance and a simplified cooling system [7–9].

However, the advantages presented by HT-PEFCs are still not promising enough for widespread utilization in industrial applications. Several challenges still must be addressed, including:

- Comprehensively studying the influence of operating conditions and material properties [10–13]
- Reducing degradation, improving durability and conducting long-time tests [14–17]
- Enhancing the sluggish oxygen reduction reaction that is related to the use of phosphoric acid as the electrolyte [18].
- Developing alternative electrolytes that do not block the Pt catalyst [18].
- Reducing catalyst loading and the cost [18].

Considering various operating conditions and material properties, conducting comprehensive experimental measurements to resolve the effects of each parameter are fairly expensive and difficult [19]. In addition, in-situ measurements for fluid flow, heat and charge transfer within the confines of PEFCs are limited. The mathematical models that are able to predict the local and

overall behaviors of PEFCs offer reliable tools for fuel cell design and optimization. With the development of high-performance computing facilities, numerical simulations can be performed with fewer constraints.

The earlier mathematical models concerning PEFCs mainly focused on conventional low temperature PEFCs with operating temperatures of 60 - 80 °C. These first studies were conducted by Springer et al. [20] and by Bernardi and Verbrugge [21]. The models developed at that time were one-dimensional (1-D), steady state and isothermal, while the principal transport phenomena were considered, including water transfer in the membrane, species transfer and electrochemical reactions. In addition, the overall cell performance was predicted and analyzed, in terms of polarization curves. These served as foundations for subsequent numerical investigations. Nguyen and White [22] provided a heat and water management model to evaluate the effectiveness of three different humidification approaches and their effects on cell operation. Meanwhile, Thampan et al. [23] developed a predictive transport model based on a dusty-fluid model that drew on the generalized Maxwell-Stefan equations. This model was capable of reliably predicting the results of membrane conductivity under various operating conditions, such as prescribed relative humidity and temperature. Marr and Li [24] implemented a simplified performance model that incorporated electrochemical reactions, cell voltage losses and reactant gas transport, where various operations and designs were studied. In turn, Berning et al. [25] developed a 3-D model that incorporated all of the major transport phenomena in the flow channels, porous electrodes and the electrolyte membrane. Lin and Beale [26], meanwhile, considered two distinct approaches and implemented them in a commercial CFD software package to evaluate the local-scale phenomena of a straight-channel and industrial PEFC designs. Correspondingly, Schwarz and Beale [27] obtained computational results for a full-scale cell design with a nonconformal unstructured mesh. All of these earlier models can be modified to studies of HT-PEFCs by neglecting the liquid water influence. However, the different electrolyte behaviors must be taken into account [7, 28, 29]. The relative humidity in the cell has an impact on the proton conductivity of the phosphoric acid as well as on the phosphoric acid doped PBI. In addition the transport mechanisms of protons in phosphoric acid are different compared to Nafion based membranes, which is why electroosmotic drag does not play a significant role with regard to water transport in an HT-PEFC. As a consequence modified models for the description of the membrane/electrolyte behavior must be implemented in HT-PEFC models.

Mathematical models of HT-PEFCs have been studied in recent years. Cheddie and Munroe [30–32] provided one of the first of these models. The work [30] presented a parametric study that represented overall cell performance in light of various geometric factors, including porous media characteristics and membrane and catalyst properties. They also carried out a 1-D mathematical model that was validated via experimental results [31]. A 3-D mathematical model was later derived [32] and also validated a model that accounted for the major transport phenomena in HT-PEFCs. Oxygen depletion and temperature variations were also presented and analyzed.

Hu et al. [33] developed a 2-D model for HT-PEFCs with a focus on the cathode side electrochemical reaction. Experimental results, including electrochemical impedance spectroscopy and polarization curves, were measured and used to validate the numerical model. This model was then used to investigate the performance degradation of fuel cells under long-term operating conditions [34]. Ubong et al. [35] employed a 3-D mathematical model to investigate the performance of HT-PEFCs under various operating conditions for temperature, pressure, and air stoichiometrical factors. In addition, experimental measurements were conducted to validate the model. Lobato et al. [36] presented neural network-based models of HT-PEFCs to investigate the effects arising from variable operating temperatures. Three types of neural network models were applied, namely by Multilayer Perceptron, Generalized Feedforward Network and a Jordan and Elman Network. They found that the Multilayer Perceptron model showed the best predictions under various thermal conditions compared to the other two. A 3-D nonisothermal HT-PEFC model was developed by Jiao and Li [37] to analyze the effects of temperature, phosphoric acid doping level and the surrounding relative humidity on cell performance. This model applied a semi-empirical correlation to compute the PBI membrane proton conductivity, which was based on an Arrhenius equation and previous experimental data. Shamardina et al. [38] described a pseudo-2-D, steady-state and isothermal model to account for the reactant crossover through the membrane. In this work, promising results were obtained from the model by taking into account the transport processes in the catalyst layer. Chippar et al. [39] conducted an investigation of the mechanical stress of fuel cells under various clamping conditions by combining the thermal stress analysis and the computational fluid dynamics (CFD) methodology. Meanwhile, Yin et al. [12] provided a 3-D, steady-state, nonisothermal numerical model for HT-PEFCs that used a novel sulfonated polybenzimidazole membrane with the correlation from previous experimental data. Unnikrishnan et al. [40], in turn, implemented an electrochemical model for hydrogen oxidation and oxygen reduction based on elementary multi-step single electron transfer reactions. This model considered carbon monoxide adsorption and desorption and was coupled with a 2-D fuel cell model to simulate transport phenomena in single cells. In addition, mathematical models, concerning carbon monoxide effects [41–43], dynamic behavior [13, 44–47], degradation [34, 48, 49] and large scale or stacks [50–55], have attracted attention.

The application of mathematical models have mainly been aimed at improving fuel cell performance by optimizing the operating conditions, material properties and geometrical factors. Su et al. [10] conducted CFD studies on the effects of operating conditions in terms of inlet gas temperature, system pressure, and inlet gas flow rate on the cell performance. They found that better performance can be obtained by increasing the inlet temperature, system pressure or flow rate. Similarly, Ferng et al. [56] performed experimental and numerical investigations on different designs and operating conditions by means of PBI loading, operating temperature, inlet flow rate, electrode thickness and porosity, as well as phosphoric acid doping level, to improve cell performance. It was thereby shown that lower PBI loading, higher operating temperatures, thinner electrode thickness, decreased porosity and higher acid doping levels

contributed to better cell performance. Sun et al. [57] analyzed numerically the effects of operating temperature, gas diffusion layer (GDL) thickness and porosity on cell performance. It was found that overall performance can be enhanced by increasing operating temperature and GDL porosity and/or decreasing GDL thickness resulting in decreased mass transfer limitations. Chippar and Ju [58] applied a numerical model to simulate gas crossover through the membrane under various conditions, including operating current density, operating temperature, and gas crossover diffusivity. The gas crossover was found to be insignificant in new membranes. Non-uniformities, meanwhile, were observed in reactants and current density distributions due to gas crossover.

Lobato et al. [59] conducted numerical simulations on the influence of flow channel geometry on cell performance. Three types of flow field designs were compared, namely: 'serpentine', 'parallel' and 'pin'. The results showed that the 'serpentine' and 'pin' type flow fields provided higher power output, while the 'parallel' design performed the least well. Grigoriev et al. [60] numerically analyzed the optimization of the geometrical factors of the key components, bipolar plates (BPPs) and GDLs, in fuel cells. It was demonstrated that the ratio of the rib width to the sum of the width of the rib and channel was approximately in the range of 0.30 - 0.35. Sousa et al. [61] applied a 3-D isothermal and steady-state model to analyze the effect of different flow field designs on performance. The results showed that the 'pin' type flow path performed better than other designs. It was also found that the 'interdigitated' flow field exhibited the highest power output. However, a heterogeneous current density with 'hot spots' was also observed. The work of Jiao et al. [62] considered various flow channel designs and carbon monoxide poisoning effects on cell performance. Similar to the results from Sousa et al. [61], an 'interdigitated' design produced the highest power output when pure hydrogen was supplied. The carbon monoxide poisoning effects on cell performance were found to be the reverse, with the 'parallel' designs showing the least influence and the 'interdigitated' design the most affected. A novel flow field design, which was modified from the 'serpentine' design, was numerically and experimentally studied by Singdeo et al. [63]. It was observed that the new design exhibited higher uniformity in current density distribution compared to a traditional serpentine design. Various operating conditions, flow field designs, material properties, etc. were also studied.

It can be seen that numerous models have been developed in recent years. Typically these were based on one of two widely applied approaches. In the first approach, the catalyst layers were treated as thin surfaces [64], while the cell output voltage, V, is calculated with a locally two-dimensional (2-D) Kirchhoff-Ohm relationship, in terms of the ideal, or Nernst potential, $E_{\rm n}$, minus losses due to activation and Ohmic overpotentials,

$$V = E_{\rm n} - \eta_{\rm c} - Ri \tag{1}$$

where R represents the area-specific ohmic resistance, i(x,y) is the local current density, and η is the local activation overpotential. Equation 1, which employs widespread application in various forms, is typically combined with the equations for conservation of mass, species, momentum, and energy to obtain three-dimensional solutions for fuel cells. This may be seen as a reasonable approximation in thin planar membrane-electrolyte assemblies. The anodic activation overpotential is negligible compared to the cathode side. This is confirmed by the second approach in this study, where the maximum ratio of the mean values in the anode to cathode electrodes is 0.6% in the simulation range.

In the second approach, the electrodes can be treated as volumetric regions, where through-plane variations in species concentrations can be taken into account. The protonic and electronic potentials are obtained by solving a pair of coupled Poisson equations:

$$\nabla \cdot (\sigma \nabla \phi) = J_{\omega} \tag{2}$$

where $\phi(x, y, z)$ is the local protonic or electronic potential, σ represents the electric conductivity, and J_{φ} is the source/sink term due to electrochemical reactions with a unit of A cm⁻³. Equation 2 is also widely used in the research community.

Although the applications of both basic approaches abound with numerous protractors and detractors, the authors are not aware of any scientific comparisons of the two basic methodologies having been undertaken. The goal of the present work, then, is to formulate a comparison between the results of one code based on Eq. 1, and another derived from the approach of Eq. 2 for a geometry for which in-house experimental data are available. The two approaches are referred to, below, as models 1 and 2, respectively. These were implemented into the open-source library, OpenFOAM-V6 [65]. The aim of the present study is, therefore, to conduct a detailed comparison of the two approaches, with both numerical verification/comparison and experimental validation performed in this and earlier studies [64]. The fuel cell prototype considered was an inhouse design [29, 66, 67], while the experimental measurements and numerical simulations were conducted and presented in a previous study by Kvesić et al [54].

2. Numerical considerations

In the PEFC applications, the overall thickness of CL electrodes varies greatly, e.g. $20~\mu\mathrm{m}$ - $120~\mu\mathrm{m}$ [68][69]. The simplification in Model 1 assumes the catalyst electrodes as thin surfaces. This may result in significant deviations if thicker electrodes are assembled in PEFCs. Therefore, Model 2, which considers the electrodes as volumetric regions, is preferable. In addition, the 3-D nature of electron and proton transfer is taken into account.

2.1. Assumptions

The assumptions made in the present numerical models are as follows:

- The simulations are in a steady state.
- Fluid flow is laminar for both the anode and cathode sides with maximum Reynolds numbers of less than 300.
- Gases obey the ideal gas law.

- The material properties for GDLs, MEA, and BPPs are assumed to be isotropic and homogeneous.
- Change to the material properties due to compression during cell assembly is not accounted for.
- The membrane is not permeable to fuel/oxidant gases.
- The membrane conductivity is assumed to be constant.
- Water is produced in a vapor phase and only exists in this phase due to the elevated operating temperature.

2.2. Governing equations

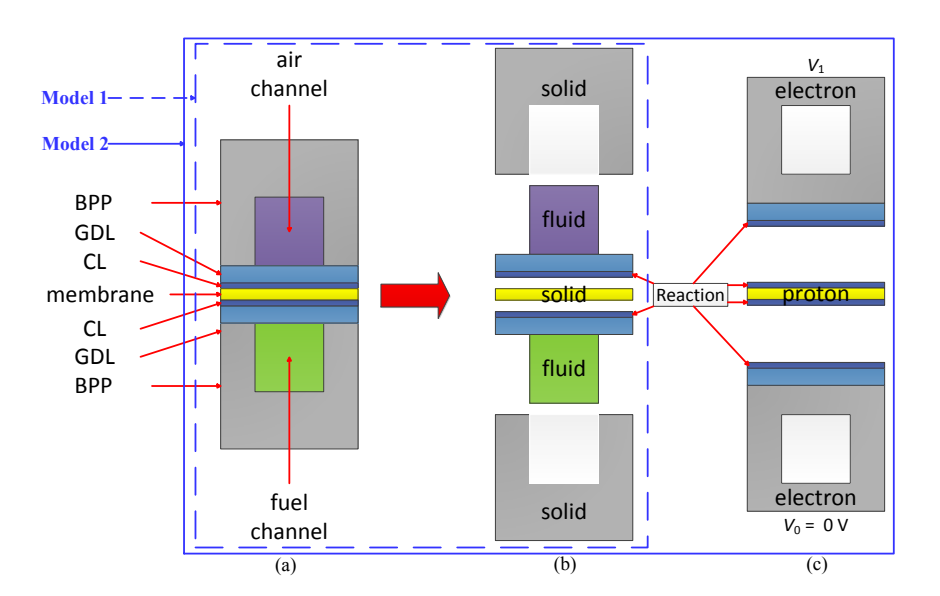


Fig. 1: Sketch of the computational domain (Model 1 and Model 2): (a) Master region; (b) sub-regions, including fluid, solid; (c) sub-regions, charged. (BPP: bipolar plate; GDL: gas diffusion layer; CL: catalyst layer)

The present study, employs multiple meshes to consider transport phenomena in different regions. Three types of sub-domains are defined: fluid, solid, and charged regions. A sketch of the computational domains is shown in Fig. 1.

The fluid region consists of air and fuel sub-regions, including flow channels and the porous media. The solid region accounts for the solid parts, by means of the membrane and BPP regions. The charged regions consider the electron and proton transfer in electrically conductive parts. In addition, the master region that represents the total fuel cell is used to solve the heat transfer, where heat sources/sinks are mapped from the appropriate sub-regions and temperatures are mapped back. It should be noted that the charged regions are only used by Model 2. Based on the simplifications in Model 1, current density is considered on 2-D catalyst surfaces rather than in the charged regions shown in Figure 1(c).

2.2.1. Fluid regions

The continuity equation This yields,

$$\frac{\partial \rho}{\partial t} + \nabla \cdot (\rho \mathbf{U}) = R_{\mathrm{m}} \tag{3}$$

where ρ is the mixture gas density, **U** represents the gas velocity, and $R_{\rm m}$ is the mass source/sink term. The transient term is neglected in steady state simulations. Moreover, the transient term $\partial/\partial t$ is always zero in steady simulations, which is also true for the following equations.

Momentum equation This takes the Darcy term into account to consider the flow in both the flow channel and porous media, which yields:

$$\frac{\partial (\rho \mathbf{U})}{\partial t} + \nabla \cdot (\rho \mathbf{U} \mathbf{U}) = -\nabla p + \nabla \cdot (\mu \nabla \mathbf{U}) + S_{D}$$
 (4)

where p is the pressure, μ represents the dynamic viscosity, and $S_{\rm D}$ is the Darcy source term, which is given by,

$$S_{\rm D} = -\frac{\mu \mathbf{U}}{K} \tag{5}$$

where K is the permeability for porous media.

Species transfer equation This accounts for the species transfer in multi-component gases, which results in:

$$\frac{\partial \left(\rho Y_{i}\right)}{\partial t} + \nabla \cdot \left(\rho \mathbf{U} Y_{i}\right) = \nabla \cdot \left(\rho D_{i}^{\text{eff}} \nabla Y_{i}\right) + R_{i} \tag{6}$$

where the subscript i means the index of species, Y is the mass fraction, $D_{\rm i}^{\rm eff}$ represents an effective diffusion coefficient, and $R_{\rm i}$ is the mass source for species i. The computation of effective values of diffusion coefficient was introduced in previous work [70].

2.2.2. Charged regions

The electron and proton transfer in these regions are only taken into account by Model 2. The general formulation of potential equation is expressed as by Eq. 2.

The current density, \mathbf{i} , is a vector that can be obtained from:

$$\mathbf{i} = -\sigma \nabla \varphi \tag{7}$$

It should be noted that the current density for Model 2 usually refers to the current density in the normal (through-cell) direction.

2.2.3. Master region

The heat transfer equation is solved on the master mesh, which is described by:

$$\frac{\partial \left(C_{p} \rho T\right)}{\partial t} + \rho \mathbf{U} C_{p} \cdot \nabla T = \nabla \cdot \left(k^{\text{eff}} \nabla T\right) + Q \tag{8}$$

where C_p is the specific heat of the gas mixture, T represents the temperature, k^{eff} is an effective thermal conductivity, and Q is the heat source. The effective thermal conductivity is calculated as follows:

$$k^{\text{eff}} = \varepsilon k_{\text{g}} + (1 - \varepsilon)k_{\text{s}} \tag{9}$$

where ε is the porosity of the porous region and $\varepsilon = 0$ in the solid regions, such as BPP and the membrane. In this study, the solid regions only provide necessary material properties for heat transfer.

2.3. Electrochemical reaction

The electrochemical reactions in PEFCs take place inside the CLs on both the anode and cathode sides.

Model 1: In HT-PEFCs, the activation overpotential at the anode side is so minor that it can be readily neglected when using pure hydrogen as fuel. Therefore, the reaction is only considered at the cathode side with a Tafel equation:

$$i = i_0 \left(\frac{C_{\rm O_2}}{C_{\rm O_2, ref}}\right)^{\gamma_c} \left[\exp\left(\frac{n\alpha_{\rm c}F}{R_q T}\eta_{\rm c}\right)\right]$$
(10)

where i_0 represents the exchange current density, with a unit of A cm⁻², C_{ref} means the reference molar concentration, γ represents the reaction order, n is the number of the electron transfer, α is the transfer coefficient, F is Faraday's constant, R_g is the universal gas constant.

The relation between the ohmic resistance R and the electric conductivity σ gives,

$$R = \frac{h}{\sigma} \tag{11}$$

where h is the thickness.

and $E_{\rm n}$ is the Nernst potential that results in the following:

$$E_{\rm n} = -\sum_{\rm i} \frac{H_{\rm i} - S_{\rm i}T}{nF} - \frac{R_g T}{nF} \ln p_{\rm i}^{a_{\rm i}}$$
 (12)

where H is enthalpy, S is entropy, p_i represents the normalized partial pressure of species i, and a_i means the stoichiometric coefficient.

In order to solve the local current density, i, Eq. 10 is inverted:

$$\eta_{\rm c} = \frac{R_g T}{n\alpha_{\rm c} F} \ln \left(\frac{i}{i_0} \left(\frac{C_{\rm O_2, ref}}{C_{\rm O_2}} \right)^{\gamma_{\rm c}} \right)$$
 (13)

Substituting Eq. 13 in Eq. 1 and defining a new function:

$$g(i) = E_{\rm n} - \frac{R_g T}{n\alpha_{\rm c} F} \ln \left(\frac{i}{i_0} \left(\frac{C_{\rm O_2, ref}}{C_{\rm O_2}} \right)^{\gamma_{\rm c}} \right) - Ri - V$$
 (14)

The local current density can therefore be obtained using Newton's method,

$$i^{n} = i^{o} - \frac{g(i)}{g(i)'}|_{i^{o}} \tag{15}$$

where the superscripts n and o refer to new and old values, respectively. It is computed iteratively until, e.g., $|i^n - i^o| < 1.0 \times 10^{-6}$.

Note: the current density is only resolved on the 2-D catalyst electrode surface, and so is the activation overpotential.

Model 2: The electrochemical reaction on the anode and cathode sides are described by Butler-Volmer equations, respectively:

$$j_{\rm a} = i_{\rm 0, a} \left(\frac{C_{\rm H_2}}{C_{\rm H_2, ref}} \right)^{\gamma_{\rm a}} \left[\exp \left(\frac{n\alpha_{\rm a}F}{R_q T} \eta_{\rm a} \right) - \exp \left(\frac{-n(1-\alpha_{\rm a})F}{R_q T} \eta_{\rm a} \right) \right]$$
(16)

$$j_{\rm c} = i_{\rm 0, c} \left(\frac{C_{\rm O_2}}{C_{\rm O_2, ref}} \right)^{\gamma_{\rm c}} \left[\exp\left(-\frac{n\alpha_{\rm c} F}{R_g T} \eta_{\rm c} \right) - \exp\left(\frac{n(1 - \alpha_{\rm c}) F}{R_g T} \eta_{\rm c} \right) \right]$$
(17)

where i_0 represents the exchange current density. The calculation of activation overpotential η yields,

$$\eta_{\rm a} = \phi_E - \phi_P - E_{\rm n, a} \tag{18}$$

and

$$\eta_{\rm c} = \phi_E - \phi_P - E_{\rm n, c} \tag{19}$$

where the subscripts P and E represent the proton and electron, respectively. In case of pure hydrogen, the reference concentration $C_{\rm H_2, \, ref}$ equals the local hydrogen concentration $C_{\rm H_2}$ because there is no other species present. The model parameters α and exchange current density i_0 have been obtained by a fit to the experimental polarization curve in the Tafel region ($i < 0.2 \, {\rm A \, cm^{-2}}$). The ohmic resistance was obtained from impedance spectroscopy.

2.4. Source terms

The source terms of the governing equations in the present study are summarized in Table 1.

2.5. Boundary conditions

Boundary conditions are important in numerical simulations. The prescription of boundary conditions of this paper is based on the operating conditions, which are listed in Table 2. In addition, pure hydrogen and dry air are supplied at inlets under the ambient pressure and the cell is operated at a temperature of 439 K. The stoichiometric factor, λ , is defined as the ratio of the supplied fuel/oxidant to the actual amount consumed. The inlet velocity for air and fuel can be calculated by means of:

$$U = \frac{M_{\rm i} A_{\rm act} \bar{i} \lambda}{\rho X_{\rm i} A_{\rm in} nF} \tag{20}$$

where the subscript i is the index of species, representing O_2 and H_2 for air and fuel, respectively.

The potential at the bottom of the anode side is fixed, 0 V, as is shown in Fig. 1. The cell output, represented by V_1 on the cathode side, is first prescribed by a user-defined value. The fuel cell was operated under galvanostatic conditions in this study, and therefore the value of V_1 will be updated according to the mean current density at the top surface,

$$V_1^n = V_1^o + \omega(i_1 - \bar{i}) \tag{21}$$

where the superscripts, n and o, are the new value and old value, respectively, while ω is the relaxation parameter, and i_1 represents the mean current density at the top surface, while \bar{i} is the prescribed mean current density.

2.6. Computational domain

The geometry applied in this study is similar to that in the previous work of Zhang et al. [64]. Hence the computational domain is also similar, with the

Table 1: Source terms in the present study

	Model 1	Model 2	Units
$R_{\rm H_2}$ (Eq. 6)	0,4	$\begin{cases} 0, \text{ Anode flow channel \& GDLs} \\ -\frac{j_{\text{a}}M_{\text{H}_2}}{2F}, \text{ Anode CL} \end{cases}$	${\rm kg}{\rm m}^{-3}{\rm s}^{-1}$
$R_{\rm O_2}$ (Eq. 6)	0^{\dagger}	$\begin{cases} 0, \text{ Cathode flow channel \& GDLs} \\ -\frac{j_c M_{\text{O}_2}}{4F}, \text{ Cathode CL} \end{cases}$	$ m kg m^{-3} s^{-1}$
$R_{\rm H_2O}$ (Eq. 6)	0^{\dagger}	$\begin{cases} 0, \text{ Cathode flow channel \& GDLs} \\ \frac{j_c M_{\text{H}_2\text{O}}}{2F}, \text{ Cathode CL} \end{cases}$	${\rm kg}{\rm m}^{-3}{\rm s}^{-1}$
$R_{\rm m}$ (Eq. 3)	0,4	$\begin{cases} 0, \text{ Flow channel \& GDLs} \\ \sum_{i} R_{i}, \text{ CLs} \end{cases}$	$ m kg m^{-3} s^{-1}$
$J_{\varphi, E}$ (Eq. 2)	_	Model 2 $\begin{cases} 0, \text{ Anode flow channel & GDLs} \\ -\frac{j_{a}M_{\text{H}_{2}}}{2F}, \text{ Anode CL} \\ 0, \text{ Cathode flow channel & GDLs} \\ -\frac{j_{c}M_{\text{O}_{2}}}{4F}, \text{ Cathode CL} \\ 0, \text{ Cathode flow channel & GDLs} \\ \frac{j_{c}M_{\text{H}_{2}\text{O}}}{2F}, \text{ Cathode CL} \\ 0, \text{ Flow channel & GDLs} \\ \sum_{i} R_{i}, \text{ CLs} \\ \int_{a}, \text{ Anode CL} \\ -j_{c}, \text{ Cathode CL} \\ 0, \text{ Other regions} \\ -j_{c}, \text{ Anode CL} \end{cases}$	$ m Am^{-3}$
$J_{\varphi, P}$ (Eq. 2)	_	$\begin{cases} -j_{\rm a}, \text{ Anode CL} \\ j_{\rm c}, \text{ Cathode CL} \\ 0, \text{ Other regions} \end{cases}$	$\mathrm{A}\mathrm{m}^{-3}$
Q (Eq. 8)	$\begin{cases} \frac{\left(-\frac{\Delta H}{2F} - V\right)i}{h}, \text{ Membrane}^* \\ 0, \text{ Other regions}^* \end{cases}$	$\begin{cases} \frac{ \mathbf{i} ^2}{\sigma}, \text{ Membrane & GDLs & BPPs} \\ j\left(\eta - \frac{\Delta ST}{nF}\right) + \frac{ \mathbf{i}_E ^2}{\sigma_E} + \frac{ \mathbf{i}_P ^2}{\sigma_P}, \text{ CLs} \\ 0, \text{ Other regions} \end{cases}$	$ m Wm^{-3}$

 $^{^\}dagger$ The mass flux due to electrochemical reaction is prescribed on the electrochemical reaction surfaces as boundary conditions, therefore, the mass source/sink terms are zero.

^{*} Assumption: the heat source, including electrochemical and Joule heating, distributes uniformly in the membrane and it is neglected in the GDLs and BPPs.

Table 2: Operating conditions

Value	Unit
101325	Pa
101325	Pa
2	_
2	_
439	K
	101325 101325 2 2

flow field as shown Fig. 2. More detailed information can be found in Kvesić et al [54]. The schematic of the cross-section for the computational domain is also shown in Fig. 1. In turn, the geometrical information for constructing the computational domain is listed in Table 3.

Table 3: Geometry information

Description	value	Unit
Active area	$212.8 (19.0 \times 11.2)$	cm^2
Channel width	1.0	mm
Channel height	1.0	mm
Rib width	1.0	mm
GDL thickness	0.28	mm
CL thickness	0.02	mm
Membrane thickness	0.05	mm

The computational mesh consists of 48.2×10^6 hexahedral elements, which were constructed using a commercial software package, ANSYS ICEM-CFD [71]. The domain was decomposed manually using a contiguous multi-block approach and the mesh was body-fitted to the serpentine flow fields and concentrated near the walls. Grid independence studies have been conducted previously [72]. The

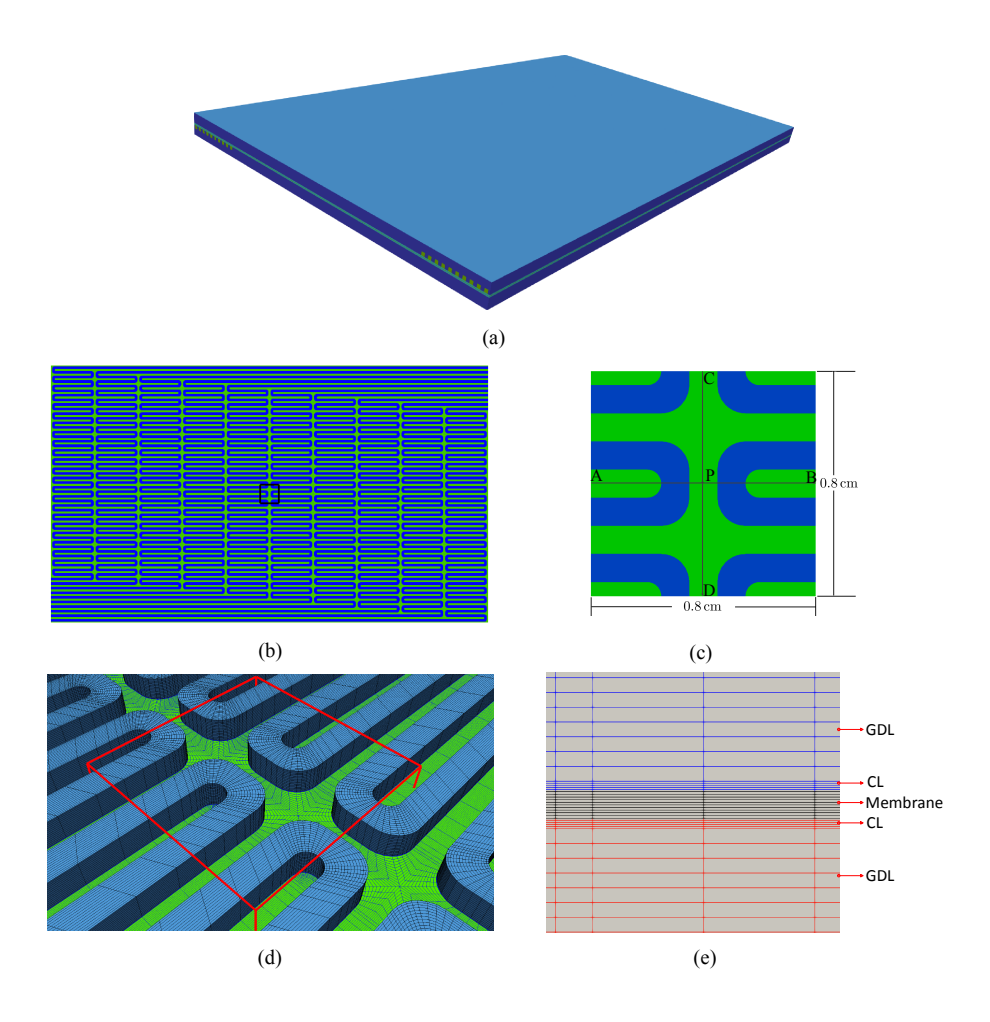


Fig. 2: Computational domain: (a) Geometry; (b) flow field (reprinted from Zhang et al. [64]); (c) sub-zone; (d) local computational grid (reprinted from Zhang et al. [64]); (e) local cross-section grid.

sub-regions referred to in this work include 'air', 'fuel', 'BPPs', 'membrane', 'electronic', and 'protonic' media, where the former four sub-regions are used in Model 1 and previous work [70]. In Model 2, the 'electronic' medium consists of the electron transfer fields on both sides, including BPPs, GDLs and CLs; meanwhile, the 'protonic' medium includes the anode CL, cathode CL and membrane.

2.7. Computational procedure

The numerical discretizations and calculations were conducted with the open source library, OpenFOAM-V6 [65]. Both models have been implemented in the latest version of OpenFOAM, which allows for large parallel calculations. All of the numerical simulations were performed at the Jülich-Aachen Research Alliance High-performance Computing (JARA-HPC) facility. Approximately 24 hours were consumed for Model 1, while 72 hours were needed for Model 2, with simulations performed for each case using 720 cores.

In conducting the numerical calculations, two linear algebraic systems (symmetric and asymmetric) were discretized from the governing equations and solved. The symmetric system was computed via conjugate gradient with an incomplete Cholesky preconditioning (ICCG) solver. The asymmetric system, in turn, was solved with a Biconjugate gradient solver Bi-CGStab. To solve the pressure-velocity coupling system discretized from the momentum transfer equation, a PISO [73] algorithm, which is an extension of the SIMPLE [74] algorithm, was utilized.

3. Results

The material properties and electrochemical parameters applied in this study are the same as in a previous one [64]. with the values listed in Table 2. The properties of O₂, N₂, H₂O, and H₂, including enthalpy, entropy, and specific heat, are expressed as polynomials, the coefficients of which can be found in the work of McBride et al. [75]. The viscosity and thermal conductivity of each gas component can be described with Sutherland's Formula [76].

Table 4: Material properties and model parameters.

Description	value	Unit
Reference concentration (C_{ref})	$\begin{cases} 6.47 & O_2 \\ 28.15 & H_2 \end{cases}$	$\mathrm{mol}\mathrm{m}^{-3}$
Exchange current density (i_0) [54]	$\begin{cases} 2.5 \times 10^4 & \text{cathode} \\ 1.0 \times 10^8 & \text{anode} \end{cases}$	${ m Am^{-3}}$
Transfer coefficient (α) [54]	$\begin{cases} 6.47 & O_2 \\ 28.15 & H_2 \end{cases}$ $\begin{cases} 2.5 \times 10^4 & \text{cathode} \\ 1.0 \times 10^8 & \text{anode} \end{cases}$ $\begin{cases} 0.35 & \text{cathode} \\ 0.5 & \text{anode} \end{cases}$ $\begin{cases} 1 & \text{cathode} \\ 1 & \text{anode} \end{cases}$	_
Reaction order (γ)	$\begin{cases} 1 & \text{cathode} \\ 1 & \text{anode} \end{cases}$	_
Electronic/protonic conductivity (σ) [54, 64]	$\begin{cases} 1 & \text{anode} \\ 20000 & \text{BPPs} \\ 5000 & \text{GDLs} \\ 2000 & \text{CLs} \\ 5 & \text{membrane} \\ \end{cases}$ $\begin{cases} 0.7 & \text{GDLs} \\ 0.2 & \text{CLs} \\ 1.0 \times 10^{-12} \end{cases}$	${ m Sm^{-1}}$
Porosity (ε) [64]	$\begin{cases} 0.7 & \text{GDLs} \\ 0.2 & \text{CLs} \end{cases}$	_
Permeability of porous media (K) [64]	1.0×10^{-12}	m^2
Thermal conductivity (k) [64]	$\begin{cases} 1.2 & \text{GDLs} \\ 0.95 & \text{membrane} \\ 20 & \text{BPPs} \end{cases}$	${ m W}{ m m}^{-1}{ m K}^{-1}$
Specific heat (C_p) [64]	$\begin{cases} 568 & \text{GDLs} \\ 1650 & \text{membrane} \\ 1580 & \text{BPPs} \end{cases}$	$ m Jkg^{-1}K^{-1}$

3.1. Polarization curves

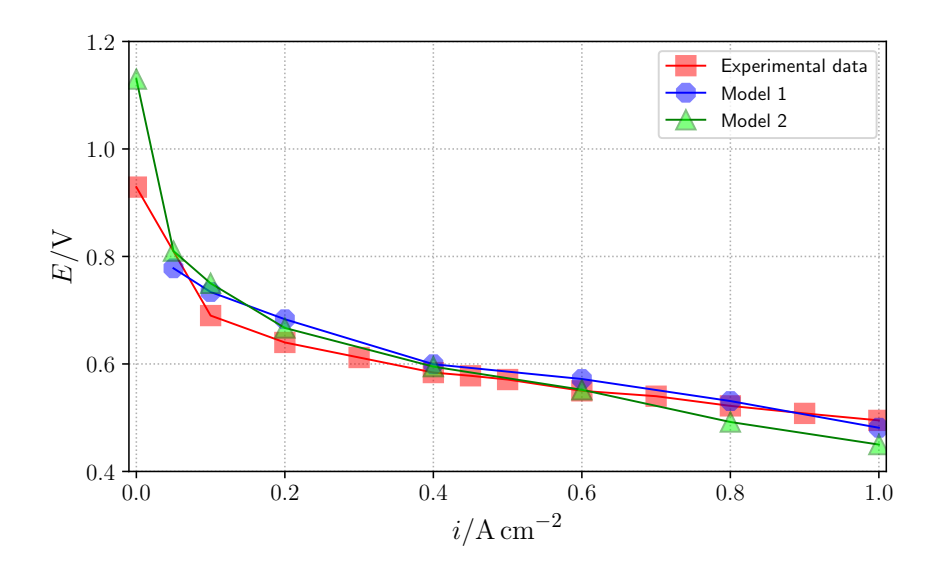


Fig. 3: Polarization curves of experimental data [54] and numerical results [64].

The polarization curves from the measured experimental results, as well as the numerical values based on the calculated results from models 1 and 2 are shown in Fig. 3. It can be seen that all the polarization curves are similar in terms of predicted voltages with slight deviations between experimental measurements and numerical simulations. Given that the experimental error is estimated to be 5%, the numerical predictions deviations are reasonable. The experimental measurements [77] are obtained from the five-cell short stack, while the present numerical studies are performed on a single cell, which approximates the middle cell of the short stack. Similar to Model 1, Model 2 predicts slightly higher voltages in lower current density conditions, the reason for which were discussed in Zhang et al. [64]. As a Tafel relation, Eq. 10, is applied in Model 1, and the simulations cannot be conducted under very low current density loads. In Model 2, however, the Butler-Volmer relation, Eqs. 16 and 17, is taken into account. Therefore, calculations may be performed close to the open circuit condition. Within the region of very low current density $(i < 0.2 \,\mathrm{A\,cm^{-2}})$, there is no notable difference between the Tafel and Butler-Volmer formulation. Obviously, the resulting overpotential is high enough to fulfill the condition of the Tafel approximation under all circumstances considered. The open circuit value is not implemented in either models, rather the Nernst potential for gas phase reaction is prescribed in Eqs. 1, 18, and 19. It is well-known that the actual open circuit potential is lower than the Nernst potential in PEFCs. A detailed discussion is considered beyond the scope of this paper, but the interested reader is referred to the study by Reimer et al. [78]. Nevertheless, the reasonable agreement between the numerical simulations and experimental results demonstrate the capability of both models to predict the overall cell performance.

3.2. Current density in the MEA

While the overall performance may readily be predicted by both models with similar results, comparisons of local values are important for evaluating the performance of fuel cells. The current density distributions on the active cell area as measured with a current scan shunt [79], as well as the numerical predictions of this work, are shown in Figure 4. Figure 4(a) shows the current density distribution predicted by Model 1, while Figs. 4(b) and 4(c) present those values at the center of the membrane and cathode catalyst electrode, respectively, as obtained using Model 2. The total current density in the catalyst electrode consists of protonic and electronic current densities, which are computed as:

$$\mathbf{i} = \mathbf{i}_P + \mathbf{i}_E \tag{22}$$

It can be observed that the general current density distributions predicted by numerical simulations using the two approaches are fairly similar to each other and also in good agreement with the experimental measurements. Due to the consumption of oxygen and the production of water vapor on the cathode side, the oxygen concentration decreases, whereas the water vapor concentration increases. This results in higher electrochemical reaction rates near the inlet region and lower rates at the outlet region. Qualitatively and quantitatively speaking, both models are capable of predicting the local current density variations for the fuel cell utilized in the present study.

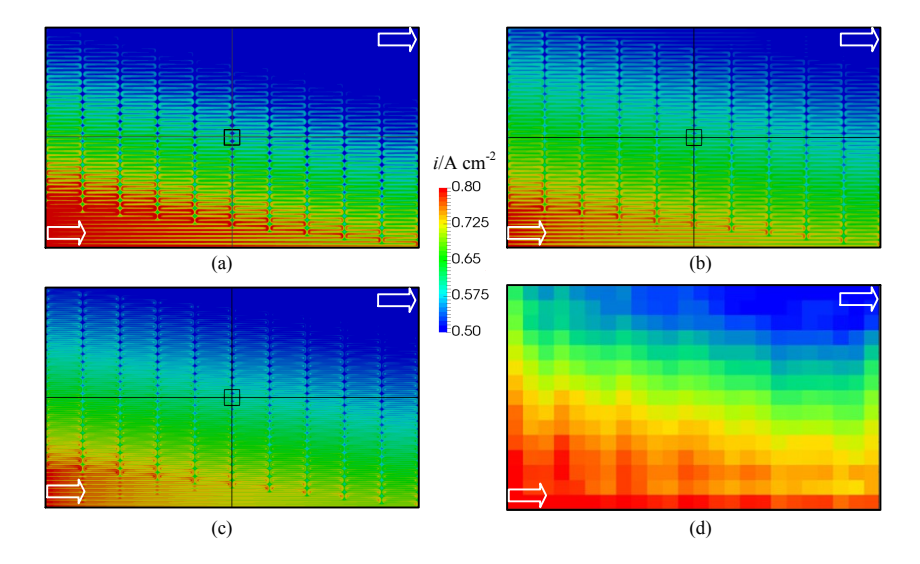


Fig. 4: Global current density distributions, $\bar{i} = 0.6\,\mathrm{A\,cm^{-2}}$. (a) Model 1, CL/membrane interface, protonic current density; (b) Model 2, membrane center, protonic current density; (c) Model 2, center of cathode CL, sum of protonic and electronic current density; (d) Experimental results [54, 80], backside (side facing away from the MEA) of the BPP, electronic current density. (arrow: air flow direction)

Differences are observed between the current densities at the center of the membrane and catalyst electrode, as shown in Figs. 4(b) and 4(c). However, these deviations only exist locally, whereas the global current density distributions are very similar. This is true considering that the results are exhibited at a current density load of $\bar{i}=0.6\,\mathrm{A\,cm^{-2}}$, in which concentration losses during gas diffusion in the CLs are fairly small. In Model 1, the current density was considered uniform through the MEA (membrane and the thin electrodes). The comparison between the numerical results and experimental results, reveals that both models can readily provide the local current density distribution in the present fuel cell under normal current density loads.

The statistical moments for the current density distribution are shown in Fig. 5. It can be seen that Model 2 exhibits a more uniform current density distribution, whereas Model 1 presents higher maximum values and lower minimum values.

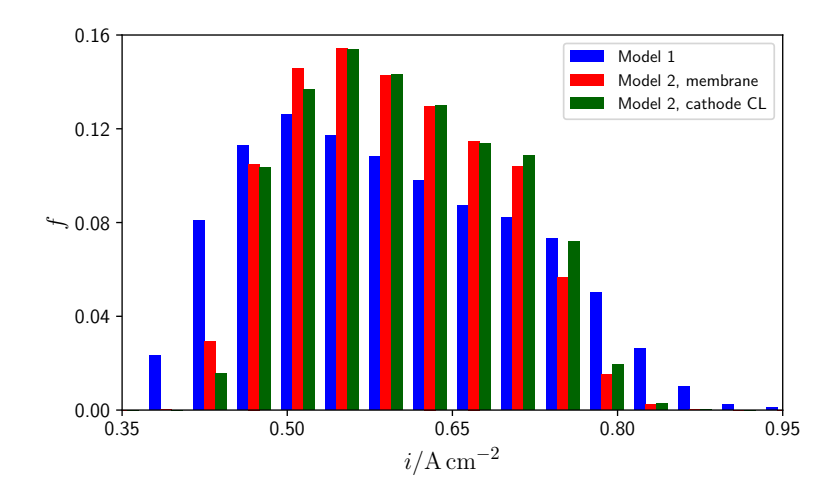


Fig. 5: Relative frequency for local current density, $\bar{i} = 0.6\,\mathrm{A\,cm^{-2}}$.

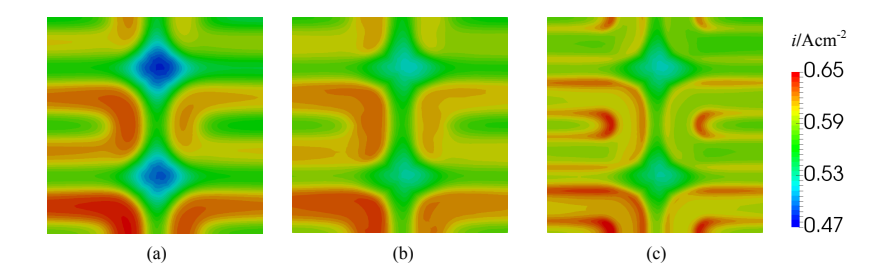


Fig. 6: Local current density distribution in the sub-regions for Model 1 and Model 2 simulation results, $\bar{i}=0.6\,\mathrm{A\,cm^{-2}}$. (a) Model 1, CL/membrane interface, protonic current density; (b) Model 2, membrane center, protonic current density; (c) Model 2, cathode CL center, sum of protonic and electronic current density, Eq. 22.

The sub-scale local current density distributions are shown in Fig. 6 by selecting a sub-region, as shown in Fig. 2. It can be seen that local current density variations can be reasonably predicted by both models. Local minima are in good agreement for the current density in the center of the membrane predicted by Model 1, Fig. 6(a), and that by Model 2, Fig. 6(b). Local minima are also observed for the current density in the catalyst electrode, as shown in Fig. 6(c). Model 1, however, predicts slightly lower local minima compared to the results obtained by Model 2. Local maxima in the membrane are found

to be similar for both models. However, they are located under the edges of ribs rather than under the gas channels for the current density in the catalyst electrode, as presented in Fig. 6(c). This is due to the higher in-plane electronic conductivity in the catalyst electrodes.

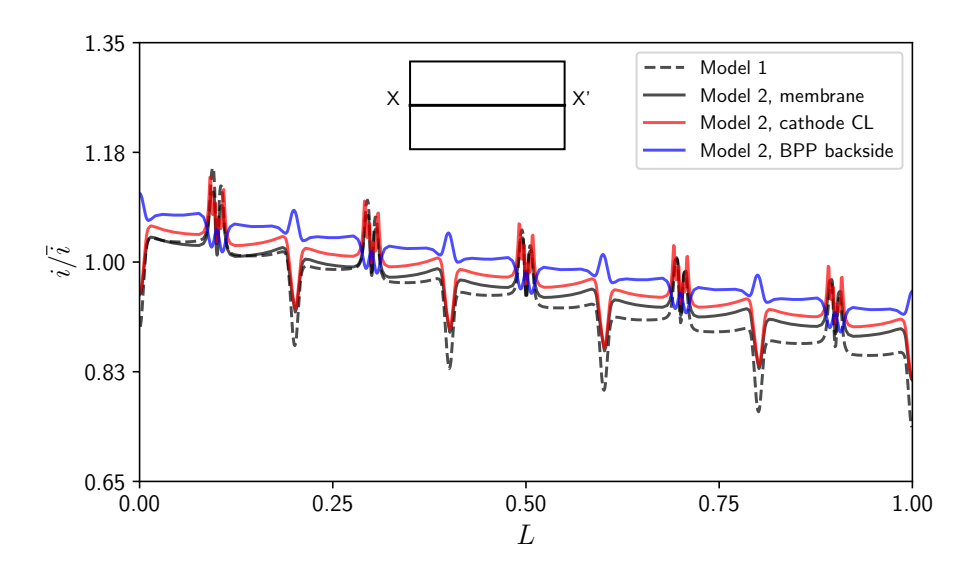


Fig. 7: Current density along cross-line XX', $\bar{i}=0.6\,\mathrm{A\,cm^{-2}}.$

The current density variations along two cross-lines, also marked in Fig. 4, are shown in Figs. 7 and 8, respectively. It can be seen that the local variations are similar to the results presented in the MEA for both models. Model 1 provides slightly larger local variations compared to those predicted by Model 2. Nevertheless, both models present similar current density distributions locally and globally.

The current density distributions through the MEA are displayed in Fig. 9 along a line perpendicular to point P (see Fig. 2(c)). As the catalyst electrodes are assumed to be thin surfaces in Model 1, current density variations through the MEA disappears. The local current density is constant and the thickness has no real meaning for Model 1. The variations of electron and proton current density are presented in Model 2. In the membrane, only protons are transferred from the anode side to the cathode side, which is very close to the value predicted

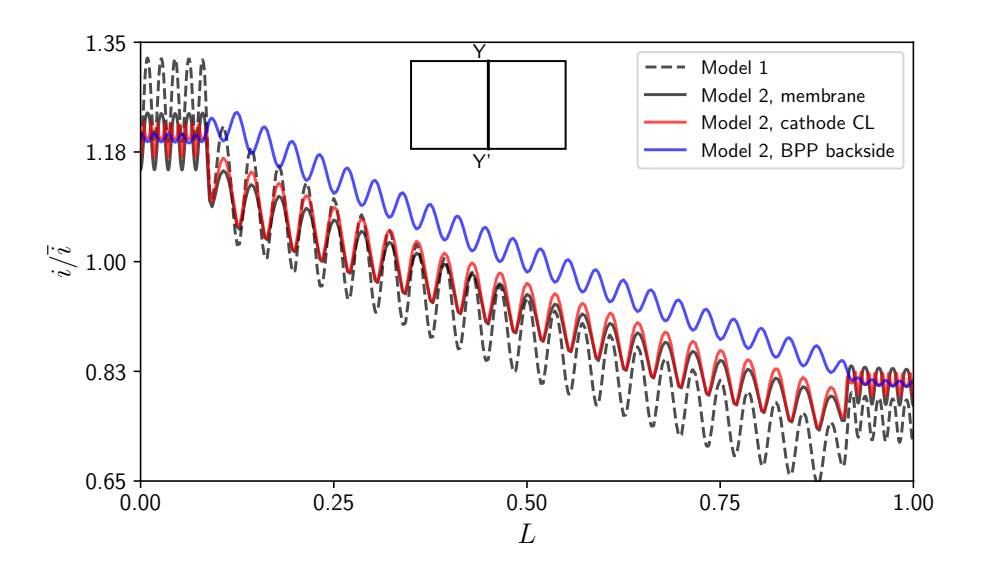


Fig. 8: Current density along cross-line YY', $\bar{i}=0.6\,\mathrm{A\,cm^{-2}}.$

in Model 1. The proton current density reaches maximum values, whereas those of the electron are always zero. In the electrodes, proton transfer occurs in the presence of the polymer electrolyte. The proton/electron current density decreased/increased going from the membrane to the GDL, respectively. In the GDLs and BPPs, only electron transfer takes place.

The reactant concentration variations in both the anode and cathode CLs are important features that are captured by Model 1. As is shown in Fig. 9, the difference of current density variation between the anode and cathode sides reveals that species concentration gradients result due to the electrochemical reaction. In order to elucidate these variations in the CLs, Fig. 10 shows the reactants molar concentration in the CLs (from the membrane to the GDLs). As is expected, the H₂ concentration is nearly constant with a very small slope. The obvious variations of O₂ concentration results from the reaction consumption, the mean gradient of which is 4 mol m⁻³ mm⁻¹. The difference through the CL is 2.5%, which is minor provided there is a relative thin catalyst electrode. However, this leads to apparent current density variations through the CL. The deviations may be great for thicker CLs, especially with high current densities.

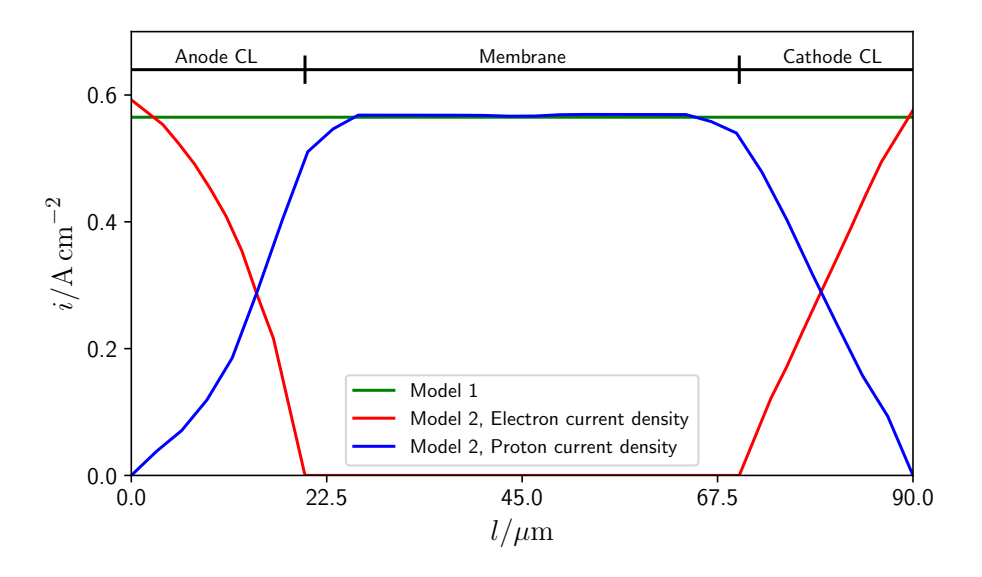


Fig. 9: Current density in the MEA, $\bar{i}=0.6\,\mathrm{A\,cm^{-2}}$. Note: in Model 1, the current density is constant and the thickness has no significance.

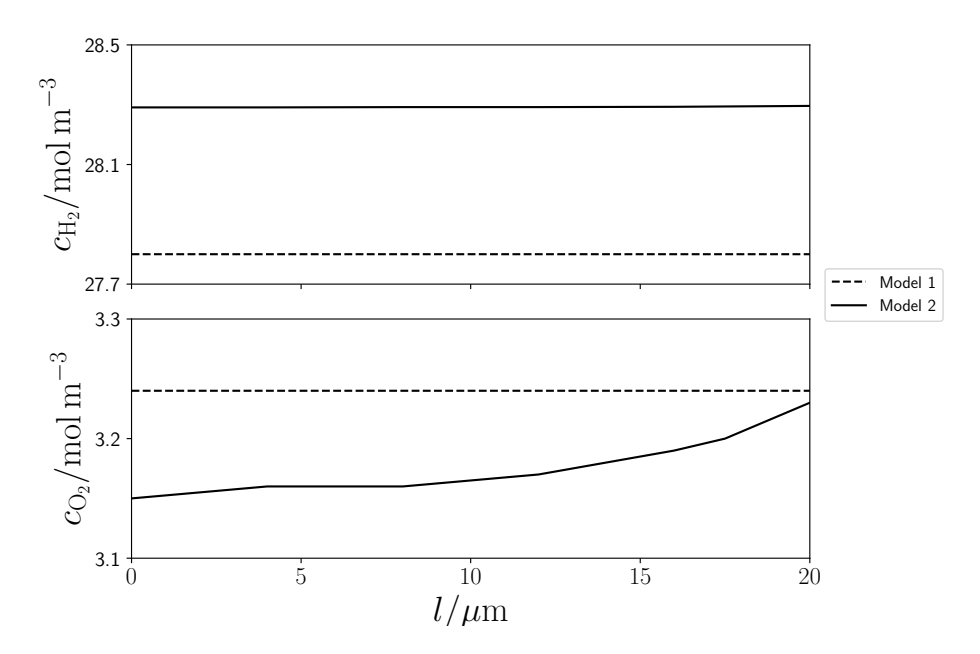


Fig. 10: Reactants concentrations in the CLs (membrane \rightarrow GDL), $\bar{i}=0.6\,\mathrm{A\,cm^{-2}}$. Note: in Model 1, the H₂ and O₂ molar concentrations are constant and the thickness has no significance.

The reactants concentration difference between Model 1 and Model 2 is within 1.7%. Hence, given $\bar{i} = 0.6 \,\mathrm{A\,cm^{-2}}$, the effects due to different treatments of CLs are still minor.

3.3. Current density in the BPPs: Model 2

When conducting the experimental measurements, the current scan shunt was located on the backside of the BPPs to mitigate their influence on cell operation [80]. The numerical predictions presented in Fig. 4 were all taken inside of the cell: Model 2 considered the results from the middle of the membrane and the cathode catalyst electrode, while the Model 1 results [64] were selected from the membrane-electrode interface. To represent the smearing effects of BPPs [80, 81], the current density distributions at the BPPs backsides are shown in Fig. 11. Compared to the current density in the membrane (Fig. 4(a)), it can be seen that the distributions at the BPPs backsides are more uniform. Nevertheless, the global tendencies of the anodic and cathodic current density distributions exhibit reasonable agreement with the experimental data, as is shown in Fig. 4(c).

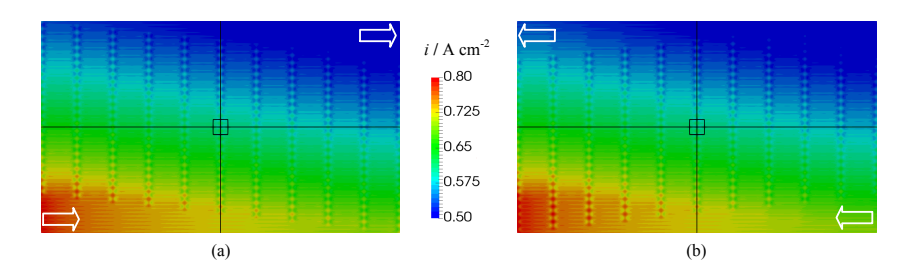


Fig. 11: Current density distributions of the BPPs backsides for Model 2, $\bar{i}=0.6\,{\rm A\,cm^{-2}}$. (a) cathode side; (b) anode side.

The smearing effects are not only found in the global current density distributions, but also local values. The sub-zone is selected to illustrate the smearing effects of the BPPs, where the sub-zones were shown in Figs. 2. The local variations are almost identical for both sides. Both results present much more uniform current density distributions, which can be clearly seen in Figs. 12(a,b).

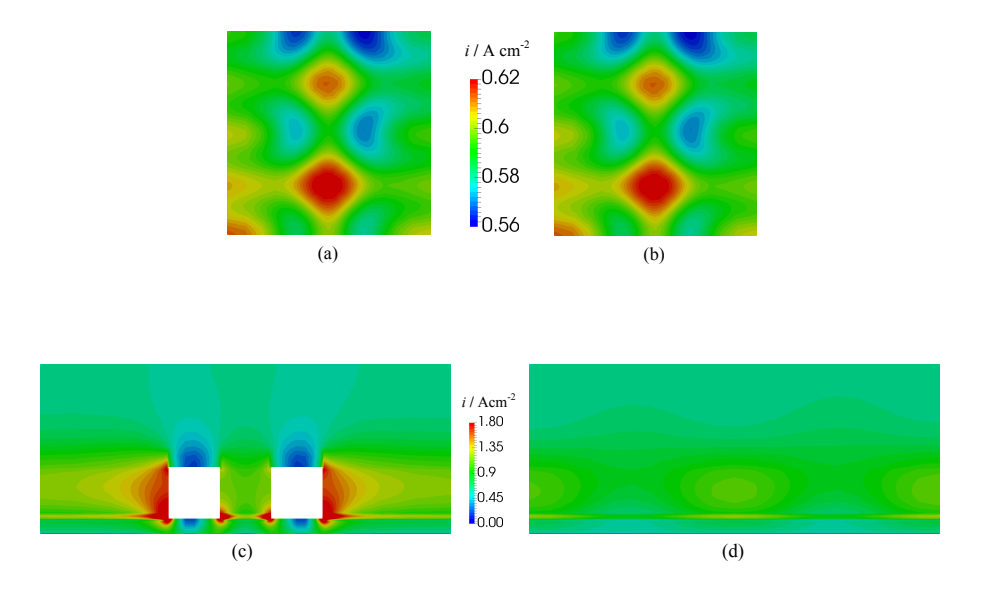


Fig. 12: Local current density distributions on the sub-zone of the BPPs for Model 2, $\bar{i}=0.6\,{\rm A\,cm^{-2}}$. (a) Cathode side; (b) Anode side; (c) Section AB; (d) Section CD. (See Fig. 2(c)

The local maximum and minimum values can still be distinguished, with the local maximum values to be found above and below the land regions, and the local minimum values above and below the channel regions, for the cathode and anode BPPs backsides, respectively. As presented in Figs. 12(a,b), the current density distribution in the membrane is different. The local minimum current densities are observed at the locations furthest from the gas channels, while the local maxima are detected at the locations closest to the gas channels. In other words, the local maximum values are located under the channel and the minimum values under the lands.

The local variations are also plotted for current density variations along two cross-lines in Figs. 7 and 8. It can be seen that the current density values on the cathode BPP backside are higher than those in the MEA for both cases. Additionally, the local maxima and minima are reversed for the current density between those on the cathode BPP backside and in the MEA.

To account for the smearing effects of BPPs, two planes, namely AB and

CD, as marked in Fig. 2(c), are selected from the electronic region. The current density distributions in the through-plane direction are shown in Fig. 12(c,d). It is easy to see the significant influence on the current density distribution due to the presence of the gas channels. The gas channels are electrical insulators, through which the electrical current cannot pass, i.e., the electrical current flows around the gas channels, which leads in turn to very high current densities at the side edges. The current density in the regions above the gas channels are smaller compared to those above the lands. Fig. 12(d) presents the current density through the land region, where the distribution is more uniform. Considering that the electrical conductivity of the porous GDLs and BPPs are very high, as well as the presence of the gas channels, current density distributions on the BBPs backsides are smeared, therefore, local properties (current density distribution and local extrema) are also altered.

4. Discussion

The two HT-PEFC models utilized in this study show the ability to predict the overall cell performance and local current density distributions. The present work provides new simulation results building on previous studies [64, 82]. While the simpler Model 1 neglected the influence of BPPs on the current density distributions, Model 2 shows smearing effects due to the BPPs and gas channels. The overall cell performance and local current density distributions predicted by Model 2 show good agreement with Model 1 and the experimental data [54]. The current density distributions in the sub-zones and along the cross-lines in this study also show deviations between the membrane and BPPs backsides. To measure the current density distribution, the current scan shunt is usually placed between the BPPs and current collectors so that the fuel cell's operation is not affected. Hence, the experimentally measured current density represents the values on the BPPs backsides. The general current density distributions can be readily captured by this methodology. However, local values on the BPPs backsides may be significantly altered.

In the present study, the GDL is assumed to be homogeneous, isotropic, and without compression. During cell assembly, it is estimated that the mechanical compression of the GDLs may be as high as 16 - 20 %. As is shown in the study by Froning et al. [83], the effect of uneven compression was found to be a function of the channel-to-rib width ratio, which was an important consideration in fuel cell design and optimization. The work of Wang et al. [84] showed current density variations due to the GDL compression, with the authors finding that the intrusion of GDLs into the gas channel provided additional contact area for electron transfer. The effects of the anisotropic GDLs on the current density distributions were studied by Randrianarizafy et al. [85]. The GDL compression and heterogeneous properties are also important factors in the numerical simulations [86, 87]. Additional work should therefore be conducted to address this issue in the future.

Model 2 provides additional information about the electric current fields in the computational domain, while Model 1 only provides a 2-D current density distribution due to the thin catalyst electrode assumption. The local reactant concentration variations through the catalyst electrodes can only be accounted for by Model 2, where the electrodes are treated as volumes. In this study, it can be seen that an oxygen concentration gradient exists in the cathode CL when $\bar{i} = 0.6 \,\mathrm{A\,cm^{-2}}$. They may cause deviations of current density distribution between Model 1 and Model 2. The deviations might be significant as the species concentration gradient in the CL increases and the concentration overpotential is also large, if thicker catalyst electrodes are applied and/or higher current densities are prescribed. It is to be noted that in Model 1, the reactant and product concentrations are taken at locations immediately adjacent to the MEA. In hindsight, it might have been better if these values are obtained at the center of the CL through planes (the CLs in Model 1 are discretized as passive nonreacting porous media, similar to the GDLs). Thus, only if the reaction orders, $\gamma_{\rm c}$ in Eqs. 17 and 10, and $\gamma_{\rm a}$ in Eq. 16 differ significantly from unity would one anticipate a difference between the two models. Of course, when the values of the exchange current, i_0 , become very large (see Table 4), the anodic overpotential becomes negligibly small. The reader will note that the Tafel equation, Eq. 10, and Butler-Volmer equations, Eqs. 16 and 17 generate similar results for the operating conditions prescribed here. If the current density is so large that local starvation occurred in the CLs, neither model will predict the current density as the underlying assumption of a simple hydrogen-oxygen reaction is violated. PEFCs are not generally operated in this regime which rapidly leads to degradation and failure.

In performing the numerical calculations, Model 2 typically consumes approximately three times the computational resources of Model 1. Under normal operating conditions, both models can readily predict the overall performance and internal current density distributions. A balance between Model 1 and Model 2 should be struck between the computational requirement and the accuracy of the predictions.

In a previous study by Cao [88], a macro-model was developed based on the work of Kulikovsky [89], with the aim of covering the gap between Model 1 and Model 2. The activation overpotential and mass fraction were integrated across the CLs in through-plan direction. This model severed as an supplementary model for Model 1 by taking the transport properties of protons and oxygen in the CLs into consideration. It was found that this model predicted similar results with Model 1, however, with an exception that it showed more homogeneous current density distribution. This is somehow similar in the present study while considering the comparison between Model 1 and Model 2. Although there still exist some limitations in the macro-model, e.g. different values of transfer coefficient, nonisotropic CLs, etc., Cao's model offers valuable information on how to conduct both more accurate and less expensive simulations. Therefore, future studies will account for the implementation and application of different empirical models derived from the work of Cao [88].

5. Conclusions

With the motivation to conduct a quantitative comparison of two state-of-the-art 3-D non-isothermal HT-PEFC models, simulations were performed on a fuel cell prototype with an active area of 200 cm-2. Model 1 was based on a Kirchhoff-Ohm (Nernst minus losses) relation, Eq. 1. Model 2 considered the 3-D distribution of electronic and protonic current densities and potentials, Eq. 2. The key findings are as follows:

- 1. The overall performance, in terms of polarization curves, when compared with experimental data, are in good agreement for both Models 1 and 2.
- 2. The current density distributions predicted by Model 2 compare closely to those simulated by Model 1 and measured experimentally, on the GDL and catalyst electrode interface and BBP backside, respectively.
- 3. Model 2 resolves the current density variation through the MEA and catalyst electrodes, and the variation of the species in the catalyst electrode(s). It also presents the local extreme current densities in/on the surface of the BPP. These are beyond the capability of Model 1.
- 4. Both models may readily be applied in HT-PEFC simulations for normal operating conditions. At high current density, and/or with thicker catalyst electrodes, Model 2 may provide more accurate predictions.

Present-day MEA assemblies are typically only a few hundred microns thick, a trend that will continue. This suggests that Model 1 is also a reasonable engineering tool. It is to be stressed that while this may be true for this particular geometry and HT-PEFC type (and by extrapolation to other high temperature fuel cells, such as solid oxide, and other high temperature electrochemical devices such as electrolyzers). A Model 2 approach may be required in, e.g. low temperature PEFCs, where, for example, there are large variations in the through-plane conductivity, due to variations in hydration. Nevertheless, this study demonstrates the similarities and differences between two currently popular CFD approaches to fuel cell modeling and will form the basis for further comparison studies in the future. As such, it presents a contribution to the

literature, to which future studies, may refer to, in comparative studies of other mathematical methods, and in the development of benchmark cases for electrochemical research programs.

Acknowledgement

Financial support was provided by the Chinese Scholarship Council, grant number 201506230130. The study was also partly funded by the Danish Council for Strategic Research within the framework of the 4M Centre. Calculations were performed on the HPC hardware of the JARA, under grant JARA0070.

References

- [1] C. Siegel, Review of computational heat and mass transfer modeling in polymer-electrolyte-membrane (PEM) fuel cells, Energy 33 (9) (2008)
 1331 1352. doi:https://doi.org/10.1016/j.energy.2008.04.015.
 URL http://www.sciencedirect.com/science/article/pii/S0360544208001163
- [2] Y. Wang, K. S. Chen, J. Mishler, S. C. Cho, X. C. Adroher, A review of polymer electrolyte membrane fuel cells: Technology, applications, and needs on fundamental research, Applied Energy 88 (2011) 981 - 1007. doi:https://doi.org/10.1016/j.apenergy.2010.09.030. URL http://www.sciencedirect.com/science/article/pii/ S0306261910003958
- [3] A. Z. Weber, R. L. Borup, R. M. Darling, P. K. Das, T. J. Dursch, W. Gu, D. Harvey, A. Kusoglu, S. Litster, M. M. Mench, R. Mukundan, J. P. Owejan, J. G. Pharoah, M. Secanell, I. V. Zenyuk, A Critical Review of Modeling Transport Phenomena in Polymer-Electrolyte Fuel Cells, Journal of The Electrochemical Society 161 (2014) F1254-F1299. doi:10.1149/2.0751412jes.

URL http://jes.ecsdl.org/content/161/12/F1254.abstract

- [4] H.-W. Wu, A review of recent development: Transport and performance modeling of PEM fuel cells, Applied Energy 165 (2016) 81 - 106. doi:https://doi.org/10.1016/j.apenergy.2015.12.075. URL http://www.sciencedirect.com/science/article/pii/ S0306261915016487
- [5] R. K. A. Rasheed, Q. Liao, Z. Caizhi, S. H. Chan, A review on modelling of high temperature proton exchange membrane fuel cells (HT-PEMFCs), International Journal of Hydrogen Energy 42 (2017) 3142 - 3165. doi:https://doi.org/10.1016/j.ijhydene.2016.10.078. URL http://www.sciencedirect.com/science/article/pii/ S0360319916330981
- [6] M. Andersson, S. B. Beale, M. Espinoza, Z. Wu, W. Lehnert, A review of cell-scale multiphase flow modeling, including water management, in polymer electrolyte fuel cells, Applied Energy 180 (2016) 757 - 778. doi:https://doi.org/10.1016/j.apenergy.2016.08.010. URL http://www.sciencedirect.com/science/article/pii/ S0306261916310972
- [7] K. Wippermann, C. Wannek, H.-F. Oetjen, J. Mergel, W. Lehnert, Cell resistances of poly(2,5-benzimidazole)-based high temperature polymer membrane fuel cell membrane electrode assemblies: Time dependence and influence of operating parameters, Journal of Power Sources 195 (2010) 2806 2809. doi:https://doi.org/10.1016/j.jpowsour.2009.10.100. URL http://www.sciencedirect.com/science/article/pii/S0378775309019776
- [8] S. Galbiati, A. Baricci, A. Casalegno, R. Marchesi, Experimental study of water transport in a polybenzimidazole-based high temperature PEMFC, International Journal of Hydrogen Energy 37 (2012) 2462–2469. doi:10. 1016/j.ijhydene.2011.09.159.
- [9] Y. Liu, W. Lehnert, H. Jansen, R. C. Samsun, D. Stolten, A

review of high-temperature polymer electrolyte membrane fuelcell (HT-PEMFC)-based auxiliary power units for diesel-powered road vehicles, Journal of Power Sources 311 (2016) 91 – 102. doi:https://doi.org/10.1016/j.jpowsour.2016.02.033.

URL http://www.sciencedirect.com/science/article/pii/S0378775316301410

- [10] A. Su, Y. Ferng, J. Shih, CFD investigating the effects of different operating conditions on the performance and the characteristics of a high-temperature PEMFC, Energy 35 (2010) 16 27. doi:https://doi.org/10.1016/j.energy.2009.08.033.
 URL http://www.sciencedirect.com/science/article/pii/S0360544209003557
- [11] P. Chippar, K. Kang, Y.-D. Lim, W.-G. Kim, H. Ju, Effects of inlet relative humidity (RH) on the performance of a high temperature-proton exchange membrane fuel cell (HT-PEMFC), International Journal of Hydrogen Energy 39 (2014) 2767 2775. doi:https://doi.org/10.1016/j.ijhydene.2013.05.115.

 URL http://www.sciencedirect.com/science/article/pii/S0360319913013475
- [12] Y. Yin, J. Wang, X. Yang, Q. Du, J. Fang, K. Jiao, Modeling of high temperature proton exchange membrane fuel cells with novel sulfonated polybenzimidazole membranes, International Journal of Hydrogen Energy 39 (2014) 13671 13680. doi:https://doi.org/10.1016/j.ijhydene.2014.04.019.
 URL http://www.sciencedirect.com/science/article/pii/S0360319914010404
- [13] J. Park, K. Min, A quasi-three-dimensional non-isothermal dynamic model of a high-temperature proton exchange membrane fuel cell, Journal of Power Sources 216 (2012) 152 161.

- doi:https://doi.org/10.1016/j.jpowsour.2012.05.054.
 URL http://www.sciencedirect.com/science/article/pii/
 S0378775312009238
- [14] J. Kim, M. Kim, B.-G. Lee, Y.-J. Sohn, Durability of high temperature polymer electrolyte membrane fuel cells in daily based start/stop operation mode using reformed gas, International Journal of Hydrogen Energy 40 (2015) 7769 7776. doi:https://doi.org/10.1016/j.ijhydene.2014.12.122.
 URL http://www.sciencedirect.com/science/article/pii/S036031991403554X
- [15] A. Kannan, A. Kabza, J. Scholta, Long term testing of startstop cycles on high temperature PEM fuel cell stack, Journal of Power Sources 277 (2015)
 312 316. doi:https://doi.org/10.1016/j.jpowsour.2014.11.115.
 URL http://www.sciencedirect.com/science/article/pii/S0378775314019727
- [16] Y. Jeon, H. Na, H. Hwang, J. Park, H. Hwang, Y. gun Shul, Accelerated life-time test protocols for polymer electrolyte membrane fuel cells operated at high temperature, International Journal of Hydrogen Energy 40 (2015) 3057 3067. doi:https://doi.org/10.1016/j.ijhydene.2015.01.010. URL http://www.sciencedirect.com/science/article/pii/S0360319915000191
- [17] H.-J. Lee, B. G. Kim, D. H. Lee, S. J. Park, Y. Kim, J. W. Lee, D. Henkensmeier, S. W. Nam, H.-J. Kim, H. Kim, J.-Y. Kim, Demonstration of a 20W class high-temperature polymer electrolyte fuel cell stack with novel fabrication of a membrane electrode assembly, International Journal of Hydrogen Energy 36 (2011) 5521 5526. doi:https://doi.org/10.1016/j.ijhydene.2011.02.014.
 - URL http://www.sciencedirect.com/science/article/pii/S0360319911003314

[18] W. Lehnert, C. Wannek, R. Zeis, Chapter 3 Trends in High-Temperature Polymer Electrolyte Fuel Cells, in: Innovations in Fuel Cell Technologies, The Royal Society of Chemistry, 2010, pp. 41–75. doi:10.1039/ 9781849732109-00041.

URL http://dx.doi.org/10.1039/9781849732109-00041

- [19] D. Úbeda, F. J. Pinar, P. Cañizares, M. A. Rodrigo, J. Lobato, An easy parameter estimation procedure for modeling a HT-PEMFC, International Journal of Hydrogen Energy 37 (2012) 11308 11320. doi:https://doi.org/10.1016/j.ijhydene.2012.04.157.
 URL http://www.sciencedirect.com/science/article/pii/S0360319912011032
- [20] T. E. Springer, T. A. Zawodzinski, S. Gottesfeld, Polymer Electrolyte Fuel
 Cell Model, Journal of The Electrochemical Society 138 (8) (1991) 2334–2342. doi:10.1149/1.2085971.
 URL http://jes.ecsdl.org/content/138/8/2334.abstract
- [21] D. M. Bernardi, M. W. Verbrugge, A Mathematical Model of the SolidPolymerElectrolyte Fuel Cell, Journal of The Electrochemical Society 139 (9) (1992) 2477-2491. doi:10.1149/1.2221251.
 URL http://jes.ecsdl.org/content/139/9/2477.abstract
- [22] T. V. Nguyen, R. E. White, A Water and Heat Management Model for ProtonExchangeMembrane Fuel Cells, Journal of The Electrochemical Society 140 (8) (1993) 2178-2186. doi:10.1149/1.2220792. URL http://jes.ecsdl.org/content/140/8/2178.abstract
- [23] T. Thampan, S. Malhotra, H. Tang, R. Datta, Modeling of Conductive Transport in ProtonExchange Membranes for Fuel Cells, Journal of The Electrochemical Society 147 (9) (2000) 3242–3250. doi:10.1149/1.1393890.

URL http://jes.ecsdl.org/content/147/9/3242.abstract

- [24] C. Marr, X. Li, An engineering model of proton exchange membrane fuel cell performance, ARI - An International Journal for Physical and Engineering Sciences 50 (4) (1997) 190–200. doi:10.1007/s007770050014. URL https://doi.org/10.1007/s007770050014
- [25] T. Berning, D. Lu, N. Djilali, Three-dimensional computational analysis of transport phenomena in a PEM fuel cell, Journal of Power Sources 106 (2002) 284 – 294. doi:https://doi.org/10.1016/S0378-7753(01) 01057-6.
 - URL http://www.sciencedirect.com/science/article/pii/S0378775301010576
- [26] Y. Lin, S. B. Beale, Numerical predictions of transport phenomena in a proton exchange membrane fuel cell, J. Fuel Cell Sci. Technol. 2 (4) (2005) 213–218. doi:10.1115/1.2039949.
- [27] D. H. Schwarz, S. B. Beale, Calculations of transport phenomena and reaction distribution in a polymer electrolyte membrane fuel cell, International Journal of Heat and Mass Transfer 52 (2009) 4074 - 4081. doi:https://doi.org/10.1016/j.ijheatmasstransfer.2009.03.043. URL http://www.sciencedirect.com/science/article/pii/ S0017931009002294
- [28] C. Wannek, W. Lehnert, J. Mergel, Membrane electrode assemblies for high-temperature polymer electrolyte fuel cells based on poly(2,5benzimidazole) membranes with phosphoric acid impregnation via the catalyst layers, Journal of Power Sources 192 (2) (2009) 258 - 266. doi:https://doi.org/10.1016/j.jpowsour.2009.03.051. URL http://www.sciencedirect.com/science/article/pii/ S0378775309005576
- [29] C. Korte, F. Conti, J. Wackerl, W. Lehnert, Phosphoric Acid and its Interactions with Polybenzimidazole-Type Polymers, Springer International Publishing, Cham, 2016, Ch. 9, pp. 169–194. doi:10.1007/

- 978-3-319-17082-4_8.
 URL https://doi.org/10.1007/978-3-319-17082-4_8
- [30] D. F. Cheddie, N. D. Munroe, Parametric model of an intermediate temperature PEMFC, Journal of Power Sources 156 (2006) 414 - 423. doi:https://doi.org/10.1016/j.jpowsour.2005.06.010. URL http://www.sciencedirect.com/science/article/pii/ S0378775305008426
- [31] D. F. Cheddie, N. D. Munroe, Mathematical model of a PEMFC using a PBI membrane, Energy Conversion and Management 47 (2006) 1490 – 1504. doi:https://doi.org/10.1016/j.enconman.2005.08.002. URL http://www.sciencedirect.com/science/article/pii/ S0196890405001937
- [32] D. F. Cheddie, N. D. Munroe, Three dimensional modeling of high temperature PEM fuel cells, Journal of Power Sources 160 (2006) 215 – 223. doi:https://doi.org/10.1016/j.jpowsour.2006.01.035. URL http://www.sciencedirect.com/science/article/pii/ S0378775306000917
- [33] J. Hu, H. Zhang, J. Hu, Y. Zhai, B. Yi, Two dimensional modeling study of PBI/H3PO4 high temperature PEMFCs based on electrochemical methods, Journal of Power Sources 160 (2006) 1026 - 1034. doi:https://doi.org/10.1016/j.jpowsour.2006.02.026. URL http://www.sciencedirect.com/science/article/pii/ S0378775306003405
- [34] J. Hu, H. Zhang, Y. Zhai, G. Liu, J. Hu, B. Yi, Performance degradation studies on PBI/H3PO4 high temperature PEMFC and one-dimensional numerical analysis, Electrochimica Acta 52 (2006) 394 401. doi:https://doi.org/10.1016/j.electacta.2006.05.020.
 URL http://www.sciencedirect.com/science/article/pii/S0013468606006141

[35] E. U. Ubong, Z. Shi, X. Wang, Three-Dimensional Modeling and Experimental Study of a High Temperature PBI-Based PEM Fuel Cell, Journal of The Electrochemical Society 156 (2009) B1276-B1282. doi: 10.1149/1.3203309.

URL http://jes.ecsdl.org/content/156/10/B1276.abstract

- [36] J. Lobato, P. Cañizares, M. A. Rodrigo, J. J. Linares, C.-G. Piuleac, S. Curteanu, The neural networks based modeling of a polybenzimidazole-based polymer electrolyte membrane fuel cell: Effect of temperature, Journal of Power Sources 192 (2009) 190 194. doi:https://doi.org/10.1016/j.jpowsour.2009.01.079.
 URL http://www.sciencedirect.com/science/article/pii/S0378775309001645
- [37] K. Jiao, X. Li, A Three-Dimensional Non-isothermal Model of High Temperature Proton Exchange Membrane Fuel Cells with Phosphoric Acid Doped Polybenzimidazole Membranes, Fuel Cells 10 (2010) 351–362. doi: 10.1002/fuce.200900059.
 URL http://dx.doi.org/10.1002/fuce.200900059
- [38] O. Shamardina, A. Chertovich, A. Kulikovsky, A. Khokhlov, A simple model of a high temperature PEM fuel cell, International Journal of Hydrogen Energy 35 (2010) 9954 - 9962. doi:https://doi.org/10.1016/j.ijhydene.2009.11.012. URL http://www.sciencedirect.com/science/article/pii/S0360319909017510
- [39] P. Chippar, K. Oh, D. Kim, T.-W. Hong, W. Kim, H. Ju, Coupled mechanical stress and multi-dimensional CFD analysis for high temperature proton exchange membrane fuel cells (HT-PEMFCs), International Journal of Hydrogen Energy 38 (2013) 7715 7724. doi:https://doi.org/10.1016/j.ijhydene.2012.07.122.

- URL http://www.sciencedirect.com/science/article/pii/S0360319912017533
- [40] A. Unnikrishnan, N. Rajalakshmi, V. M. Janardhanan, Mechanistic modeling of electrochemical charge transfer in HT-PEM fuel cells, Electrochimica Acta 261 (2018) 436 444. doi:https://doi.org/10.1016/j.electacta.2017.12.150.
 URL http://www.sciencedirect.com/science/article/pii/

S0013468617327251

- [41] K. Jiao, I. E. Alaefour, X. Li, Three-dimensional non-isothermal modeling of carbon monoxide poisoning in high temperature proton exchange membrane fuel cells with phosphoric acid doped polybenzimidazole membranes, Fuel 90 (2011) 568 582. doi:https://doi.org/10.1016/j.fuel.2010.10.018.

 URL http://www.sciencedirect.com/science/article/pii/S0016236110005582
- [42] K. Oh, G. Jeong, E. Cho, W. Kim, H. Ju, A CO poisoning model for high-temperature proton exchange membrane fuel cells comprising phosphoric acid-doped polybenzimidazole membranes, International Journal of Hydrogen Energy 39 (2014) 21915 21926. doi:https://doi.org/10.1016/j.ijhydene.2014.06.101.

 URL http://www.sciencedirect.com/science/article/pii/S0360319914017807
- [43] K. Oh, H. Ju, Temperature dependence of CO poisoning in high-temperature proton exchange membrane fuel cells with phosphoric acid-doped polybenzimidazole membranes, International Journal of Hydrogen Energy 40 (2015) 7743 7753. doi:https://doi.org/10.1016/j.ijhydene.2015.01.107.

 URL http://www.sciencedirect.com/science/article/pii/S0360319915001755

- [44] T. Sousa, M. Mamlouk, K. Scott, A dynamic non-isothermal model of a laboratory intermediate temperature fuel cell using PBI doped phosphoric acid membranes, International Journal of Hydrogen Energy 35 (2010) 12065

 12080. doi:https://doi.org/10.1016/j.ijhydene.2010.08.057.
 URL http://www.sciencedirect.com/science/article/pii/S0360319910016964
- [45] D. Singdeo, T. Dey, P. C. Ghosh, Modelling of start-up time for high temperature polymer electrolyte fuel cells, Energy 36 (2011) 6081 - 6089. doi:https://doi.org/10.1016/j.energy.2011.08.007. URL http://www.sciencedirect.com/science/article/pii/ S0360544211005378
- [46] H. S. Kim, S. W. Jeon, D. Cha, Y. Kim, Numerical analysis of a high-temperature proton exchange membrane fuel cell under humidified operation with stepwise reactant supply, International Journal of Hydrogen Energy 41 (2016) 13657 13665. doi:https://doi.org/10.1016/j.ijhydene.2016.05.296.
 URL http://www.sciencedirect.com/science/article/pii/S0360319916318201
- [47] H. Huang, Y. Zhou, H. Deng, X. Xie, Q. Du, Y. Yin, K. Jiao, Modeling of high temperature proton exchange membrane fuel cell start-up processes, International Journal of Hydrogen Energy 41 (2016) 3113 3127. doi:https://doi.org/10.1016/j.ijhydene.2015.12.134.
 URL http://www.sciencedirect.com/science/article/pii/S0360319915313902
- [48] A. H. Mamaghani, B. Najafi, A. Casalegno, F. Rinaldi, Predictive modelling and adaptive long-term performance optimization of an HT-PEM fuel cell based micro combined heat and power (CHP) plant, Applied Energy 192 (2017) 519 529. doi:https://doi.org/10.1016/j.apenergy.2016.08.050.

- URL http://www.sciencedirect.com/science/article/pii/S0306261916311370
- [49] S. Won, K. Oh, H. Ju, Numerical degradation studies of high-temperature proton exchange membrane fuel cells with phosphoric acid-doped PBI membranes, International Journal of Hydrogen Energy 41 (19) (2016) 8296 8306, special Issue on Progress in Hydrogen Production and Applications (ICH2P-2015), 3-6 May 2015, Oshawa, Ontario, Canada. doi:https://doi.org/10.1016/j.ijhydene.2015.10.153.
 URL http://www.sciencedirect.com/science/article/pii/

S0360319916308667

- [50] A. Arsalis, M. P. Nielsen, S. K. Kr, Modeling and optimization of a 1kWe HT-PEMFC-based micro-CHP residential system, International Journal of Hydrogen Energy 37 (2012) 2470 - 2481. doi:https://doi.org/10.1016/j.ijhydene.2011.10.081. URL http://www.sciencedirect.com/science/article/pii/ S0360319911024554
- [51] M. Drakselov, R. Kodm, D. nita, F. Beckmann, K. Bouzek, Three-dimensional macrohomogeneous mathematical model of an industrial-scale high-temperature PEM fuel cell stack, Electrochimica Acta 273 (2018) 432 446. doi:https://doi.org/10.1016/j.electacta.2018.04.042.
 URL http://www.sciencedirect.com/science/article/pii/S0013468618307746
- [52] P. Ribeirinha, M. Abdollahzadeh, J. Sousa, M. Boaventura, A. Mendes, Modelling of a high-temperature polymer electrolyte membrane fuel cell integrated with a methanol steam reformer cell, Applied Energy 202 (2017) 6-19. doi:https://doi.org/10.1016/j.apenergy.2017.05.120. URL http://www.sciencedirect.com/science/article/pii/ S0306261917306244

- [53] J. Park, K. Min, Dynamic modeling of a high-temperature proton exchange membrane fuel cell with a fuel processor, International Journal of Hydrogen Energy 39 (2014) 10683 10696. doi:https://doi.org/10.1016/j.ijhydene.2014.04.210.
 URL http://www.sciencedirect.com/science/article/pii/S0360319914013007
- [54] M. Kvesić, U. Reimer, D. Froning, L. Lüke, W. Lehnert, D. Stolten, 3D modeling of a 200cm2 HT-PEFC short stack, International Journal of Hydrogen Energy 37 (2012) 2430 2439. doi:https://doi.org/10.1016/j.ijhydene.2011.10.055.
 URL http://www.sciencedirect.com/science/article/pii/S0360319911024177
- [55] B. Najafi, A. H. Mamaghani, A. Baricci, F. Rinaldi, A. Casalegno, Mathematical modelling and parametric study on a 30kWel high temperature PEM fuel cell based residential micro cogeneration plant, International Journal of Hydrogen Energy 40 (2015) 1569 1583. doi:https://doi.org/10.1016/j.ijhydene.2014.11.093.
 URL http://www.sciencedirect.com/science/article/pii/S0360319914032273
- [56] Y. Ferng, A. Su, J. Hou, Parametric investigation to enhance the performance of a PBI-based high-temperature PEMFC, Energy Conversion and Management 78 (2014) 431 - 437. doi:https: //doi.org/10.1016/j.enconman.2013.10.069. URL http://www.sciencedirect.com/science/article/pii/ S0196890413007048
- [57] H. Sun, C. Xie, H. Chen, S. Almheiri, A numerical study on the effects of temperature and mass transfer in high temperature PEM fuel cells with ab-PBI membrane, Applied Energy 160 (2015) 937 944. doi:https://doi.org/10.1016/j.apenergy.2015.02.053.

- URL http://www.sciencedirect.com/science/article/pii/S0306261915002305
- [58] P. Chippar, H. Ju, Numerical modeling and investigation of gas crossover effects in high temperature proton exchange membrane (PEM) fuel cells, International Journal of Hydrogen Energy 38 (2013) 7704 7714. doi:https://doi.org/10.1016/j.ijhydene.2012.07.123.
 URL http://www.sciencedirect.com/science/article/pii/S0360319912017545
- [59] J. Lobato, P. Cañizares, M. A. Rodrigo, F. J. Pinar, E. Mena, D. Úbeda, Three-dimensional model of a 50cm2 high temperature PEM fuel cell. Study of the flow channel geometry influence, International Journal of Hydrogen Energy 35 (2010) 5510 5520. doi:https://doi.org/10.1016/j.ijhydene.2010.02.089.
 URL http://www.sciencedirect.com/science/article/pii/S0360319910003897
- [60] S. Grigoriev, A. Kalinnikov, N. Kuleshov, P. Millet, Numerical optimization of bipolar plates and gas diffusion electrodes for PBI-based PEM fuel cells, International Journal of Hydrogen Energy 38 (2013) 8557 8567. doi:https://doi.org/10.1016/j.ijhydene.2012.12.021.
 URL http://www.sciencedirect.com/science/article/pii/S0360319912026596
- [61] T. Sousa, M. Mamlouk, K. Scott, C. M. Rangel, Three Dimensional Model of a High Temperature PEMFC. Study of the Flow Field Effect on Performance, Fuel Cells 12 (2012) 566-576. doi:10.1002/fuce.201100197. URL http://dx.doi.org/10.1002/fuce.201100197
- [62] K. Jiao, Y. Zhou, Q. Du, Y. Yin, S. Yu, X. Li, Numerical simulations of carbon monoxide poisoning in high temperature proton exchange membrane fuel cells with various flow channel designs, Applied Energy 104 (2013) 21 41. doi:https://doi.org/10.1016/j.apenergy.2012.10.059.

- URL http://www.sciencedirect.com/science/article/pii/S0306261912007787
- [63] D. Singdeo, T. Dey, S. Gaikwad, S. J. Andreasen, P. C. Ghosh, A new modified-serpentine flow field for application in high temperature polymer electrolyte fuel cell, Applied Energy 195 (2017) 13 22. doi:https://doi.org/10.1016/j.apenergy.2017.03.022.
 URL http://www.sciencedirect.com/science/article/pii/S0306261917302404
- [64] S. Zhang, U. Reimer, S. B. Beale, W. Lehnert, D. Stolten, Modeling polymer electrolyte fuel cells: A high precision analysis, Applied Energy 233-234 (2019) 1094 - 1103. doi:https: //doi.org/10.1016/j.apenergy.2018.10.026. URL http://www.sciencedirect.com/science/article/pii/ S0306261918315769
- [65] The OpenFOAM Foundation, Openfoam v6 user guide, https://cfd.direct/openfoam/user-guide.
- [66] A. Bendzulla, Von der Komponente zum Stack: Entwicklung und Auslegung von HT-PEFC-Stacks der 5 kW-Klassen, phdthesis, RWTH, in German (2010).
- [67] H. Janßen, J. Supra, W. Lehnert, Stack Concepts for High Temperature Polymer Electrolyte Membrane Fuel Cells, Springer International Publishing, Cham, 2016, Ch. 20, pp. 441–457. doi:10.1007/978-3-319-17082-4_ 20.
 - URL https://doi.org/10.1007/978-3-319-17082-4_20
- [68] F. Liu, S. Mohajeri, Y. Di, K. Wippermann, W. Lehnert, Influence of the Interaction Between Phosphoric Acid and Catalyst Layers on the Properties of HTPEFCs, Fuel Cells 14 (5) (2014) 750–757. doi:10.1002/fuce. 201300272.
 - URL https://doi.org/10.1002/fuce.201300272

- [69] U. R. Salomov, E. Chiavazzo, P. Asinari, Gas-dynamic and electro-chemical optimization of catalyst layers in high temperature polymeric electrolyte membrane fuel cells, International Journal of Hydrogen Energy 40 (15) (2015) 5425 5431. doi:https://doi.org/10.1016/j.ijhydene.2015.01.059.

 URL http://www.sciencedirect.com/science/article/pii/
- [70] S. B. Beale, H.-W. Choi, J. G. Pharoah, H. K. Roth, H. Jasak, D. H. Jeon, Open-source computational model of a solid oxide fuel cell, Computer Physics Communications 200 (2016) 15 26. doi:https://doi.org/10.1016/j.cpc.2015.10.007.
 URL http://www.sciencedirect.com/science/article/pii/S0010465515003872
- [71] ANSYS, https://www.ansys.com/, accessed date: 04-06-2019.

S0360319915000981

- [72] S. Zhang, U. Reimer, Y. Rahim, S. B. Beale, W. Lehnert, Numerical modeling of polymer electrolyte fuel cells with analytical and experimental validation, Journal of Electrochemical Energy Conversion and Storage 16 (3) (2019) 031002.
- [73] R. Issa, Solution of the implicitly discretised fluid flow equations by operator-splitting, Journal of Computational Physics 62 (1) (1986) 40 65. doi:https://doi.org/10.1016/0021-9991(86)90099-9.
 URL http://www.sciencedirect.com/science/article/pii/0021999186900999
- [74] S. V. PATANKAR, D. B. Spalding, A calculation procedure for the transient and steady-state behaviour of shell-and-tube heat exchangers, Imperial College of Science and Technology, Department of Mechanical Engineering, 1972.
- [75] B. J. McBride, Coefficients for calculating thermodynamic and transport

- properties of individual species, Vol. 4513, National Aeronautics and Space Administration, Office of Management, 1993.
- [76] W. Sutherland, Lii. the viscosity of gases and molecular force, The London, Edinburgh, and Dublin Philosophical Magazine and Journal of Science 36 (223) (1893) 507–531.
- [77] L. Lüke, H. Janßen, M. Kvesić, W. Lehnert, D. Stolten, Performance analysis of HT-PEFC stacks, International Journal of Hydrogen Energy 37 (2012) 9171 9181. doi:https://doi.org/10.1016/j.ijhydene.2012.02.190. URL http://www.sciencedirect.com/science/article/pii/S0360319912005551
- [78] U. Reimer, W. Lehnert, Y. Holade, B. Kokoh, Irreversible losses in fuel cells, in: V. Hacker, S. Mitsushima (Eds.), Fuel Cells and Hydrogen - From Fundamentals to Applied Research, Elsevier, 2018, pp. 15–40.
- [79] S++ scan shunt, www.splusplus.com, accessed date: 04-06-2019.
- [80] L. Lüke, Analyse des betriebsverhaltens von hochtemperaturpolymerelektrolyt-brennstoffzellen, phdthesis, Forschungszentrum Jülich, in German (2013).
- [81] R. Eckl, R. Grinzinger, W. Lehnert, Current distribution mapping in polymer electrolyte fuel cellsa finite element analysis of measurement uncertainty imposed by lateral currents, Journal of Power Sources 154 (1) (2006) 171 - 179. doi:https://doi.org/10.1016/j.jpowsour.2005.04.004. URL http://www.sciencedirect.com/science/article/pii/ S0378775305006087
- [82] S. Zhang, S. B. Beale, U. Reimer, R. T. Nishida, M. Andersson, J. G. Pharoah, W. Lehnert, Simple and complex polymer electrolyte fuel cell stack models: A comparison, ECS Transactions 86 (13) (2018) 287–300. doi:10.1149/08613.0287ecst.
 - URL http://ecst.ecsdl.org/content/86/13/287.abstract

- [83] D. Froning, J. Yu, G. Gaiselmann, U. Reimer, I. Manke, V. Schmidt, W. Lehnert, Impact of compression on gas transport in non-woven gas diffusion layers of high temperature polymer electrolyte fuel cells, Journal of Power Sources 318 (2016) 26 34. doi:https://doi.org/10.1016/j.jpowsour.2016.03.102.
 URL http://www.sciencedirect.com/science/article/pii/S0378775316303238
- [84] J. Wang, J. Yuan, B. Sundn, On electric resistance effects of non-homogeneous GDL deformation in a PEM fuel cell, International Journal of Hydrogen Energy 42 (47) (2017) 28537 - 28548. doi:https://doi.org/10.1016/j.ijhydene.2017.09.119. URL http://www.sciencedirect.com/science/article/pii/ S0360319917337904
- [85] B. Randrianarizafy, P. Schott, M. Chandesris, M. Gerard, Y. Bultel, Design optimization of rib/channel patterns in a PEMFC through performance heterogeneities modelling, International Journal of Hydrogen Energy 43 (18) (2018) 8907 8926. doi:https://doi.org/10.1016/j.ijhydene.2018.03.036.
 URL http://www.sciencedirect.com/science/article/pii/S0360319918307675
- [86] Z. Niu, K. Jiao, Y. Wang, Q. Du, Y. Yin, Numerical simulation of two-phase cross flow in the gas diffusion layer microstructure of proton exchange membrane fuel cells, International Journal of Energy Research 42 (2) (2017) 802-816. doi:10.1002/er.3867.
 URL https://onlinelibrary.wiley.com/doi/abs/10.1002/er.3867
- [87] Z. Niu, Z. Bao, J. Wu, Y. Wang, K. Jiao, Two-phase flow in the mixed-wettability gas diffusion layer of proton exchange membrane fuel cells, Applied Energy 232 (2018) 443 - 450. doi:https://doi.org/10.1016/j.apenergy.2018.09.209.

- URL http://www.sciencedirect.com/science/article/pii/S0306261918315289
- [88] Q. Cao, Modelling of High Temperature PolymerElectrolyte Fuel Cells, phdthesis, RWTH Aachen University (2017).
- [89] A. A. Kulikovsky, A PhysicallyBased Analytical Polarization Curve of a PEM Fuel Cell, Journal of The Electrochemical Society 161 (3) (2014) F263-F270. doi:10.1149/2.028403jes.
 - ${\rm URL\ http://jes.ecsdl.org/content/161/3/F263.abstract}$